International Journal of Engineering Trends and Technology
ISSN: 2231-5381/ https://doi.org/10.14445/22315381/IJETT-V74I11P138

Volume 74 Issue 11, 595-610, November 2026
© 2026 Seventh Sense Research Group®

Original Article

Integrated STA-SMC with Droop Controllers for Harmonic Reduction in Islanded Microgrid System

Devireddy Sathish[1], Pannala Krishna Murthy[2], Narri Yadaiah[3]

[1,3]*Department of Electrical and Electronics Engineering, Jawaharlal Nehru Technological University Hyderabad, Kukatpally.*
[2]*Department of Electrical and Electronics Engineering, Jayaprakash Narayan College of Engineering, Mahabubnagar.*

[1]*Corresponding Author: data.sathish@gmail.com*

Received: 06 August 2026 Revised: 17 September 2026 Accepted: 30 September 2026 Published: 25 November 2026

Abstract *- The presence of non-linear loads in islanded Microgrids has made the operation of inverter based distributed generators a significant challenge. The conventional sliding mode control provides fast dynamic response and strong robustness, but it suffers from chattering, higher switching losses, and degraded voltage quality. To enhance the performance of islanded Microgrid system, this paper presents super twisting algorithm-based sliding mode controller is integrated with the conventional and enhanced reactive power droop controller. In contrast, this controller provides smooth, continuous control with almost zero chattering, low switching losses, and better voltage quality. The proposed controller is assessed through a performance comparison with the hysteresis voltage controller integrated with CDC and ERPDC. The proposed controller significantly reduces THD of voltage at the PCC from 4.28% to 2.65%.*

Keywords *- Distributed generators, Conventional droop controller, Enhanced reactive power droop controller, Super twisting algorithm, and Sliding mode controller.*

1. Introduction

Surveys worldwide reveal grave worries about the gradual demise of conventional power plants that only use fossil fuels [1]. As a result, it is projected that non-conventional energy sources will gradually supplant conventional power generation. These resources are frequently location-specific, large-scale centralized generation may not be feasible. Alternatively, renewable energy systems are installed in numerous geographically separated locations [1]. The small systems operate at modest power levels, usually between 25 Kw to 100 Kw, meet the requirements of serving local demands without compromising performance.

A Microgrid is a system that generates, distributes and uses power within a constrained geographic area. Numerous Distributed Energy Resources (DER) make up a Microgrid, which is primarily intended to supply electricity to nearby loads [2]. The Microgrids operate in dual modes, i.e. either connected to main utility grid or isolated with main grid.

Islanded Microgrids are useful in places with little or no grid access, as they rely on local generation and storage to operate independently [3, 4]. During grid disruptions or outages, they guarantee a steady and dependable power supply. This promotes sustainable energy access in isolated locations. This becomes crucial for vital infrastructures like hospitals, military installations and sizable manufacturing facilities [5]. By encouraging self-sufficiency and reducing reliance on traditional fuel-based generation, they also aid in the adoption of clean energy technologies. Power quality problems are more likely to affect Islanded Microgrid Systems (IMS) [6].

The Conventional Droop Control (CDC) approach is used for managing linear load distribution. It permits decentralized power sharing among sources and does not necessitate external communication links [7, 8], but all the Distributed Generators (DGs) must share the same voltage reference levels.

In Islanded Microgrid arrangements, communication-enabled approaches are employed to improve coordination in power sharing and to help bring voltage and frequency back to their desired values. Researchers have put forth a number of possible ways to guarantee appropriate load sharing in both linear and non-linear load scenarios in order to address these issues. To address these issues and improve the system's transient behaviour, improved adaptive droop control methods were introduced [9, 10].

In an IMS, the absence of grid support makes voltage regulation and harmonic control more difficult. Therefore, a hierarchical approach using primary and secondary control

This is an open access article under the CC BY-NC-ND license (http://creativecommons.org/licenses/by-nc-nd/4.0/)

layers is adopted to maintain stability and enhance power quality. Primary control is the first layer of control and operates without communication. It mainly depends on droop characteristics to distribute active and reactive power among distributed generators. The control response is fast, but it causes poor regulation of voltage and frequency. After the primary control stage, secondary control is implemented. Although slower than primary control, it significantly improves regulation accuracy and overall system performance [11].

Techniques such as virtual conductance control, virtual impedance, and virtual resistance have been proposed to address issues including circulating currents, harmonic distortion, and unequal power sharing in the system [12, 13]. Harmonic impedance regulation is achieved through a robust droop-based control approach, where a feed-forward mechanism adaptively adjusts the inverter impedance in accordance with the output power [14]. To address the limitations in robust droop controller, Enhancement of Reactive Power Droop Controller (ERPDC) [15, 16] is used to ensure that harmonic reactive power and circulating harmonic currents are evenly shared among all the DG units.

The key contributions of the research are outlined below:

- A novel integrated STA-SMC control framework is developed for effective harmonic compensation in the Islanded Microgrid System.
- The proposed controller is evaluated against integrated HVC-CDC-ERPDC in terms of harmonic distortion, dynamic response, robustness, and steady-state performance.

The drawbacks and limitations of the controllers reported in the literature are summarized as follows:

- CDC is poor voltage and frequency regulation, unequal power sharing among the DGs, performance affected by variation of line impedance.
- Improved droop control is complex parameter tuning, limited transient response.
- Robust droop controllers in islanded microgrids exhibit steady-state voltage and frequency deviations, slower transient response, and reduced power-sharing accuracy under nonlinear loads.
- Enhancement of reactive power droop control can introduce voltage deviations, slow down dynamic response, and may still result in inaccurate reactive power sharing under nonlinear loads.

The organization of the remaining sections of this manuscript is described as follows, Section 2 presents concept of an IMS composed of multiple DG units running a single linear and non-linear load, Principle of operation of IMS, Mathematical Modelling of IMS, the Section 3 presents existing control strategies for IMS, the Section 4 proposes on integrated STA-SMC with the conventional droop control combined with ERPDC, sliding surface formulation, STA-based control and STA Algorithm to the SMC for DG inverters, the Section 5 Simulation results and discussion; and Section 6 summarizes the conclusion.

2. Islanded Microgrid System

An islanded Microgrid is a self-contained power system that operates independently from main utility grid, generating, distributing, and consuming its own electricity. The islanded mode allows it to continue providing power to its local loads, such as buildings and facilities, even when the main grid goes down. This operating condition is especially beneficial in locations where the grid is absent, including isolated villages and island regions. During islanded operation, the Microgrid depends entirely on internal generation units and storage resources to supply the required load demand.

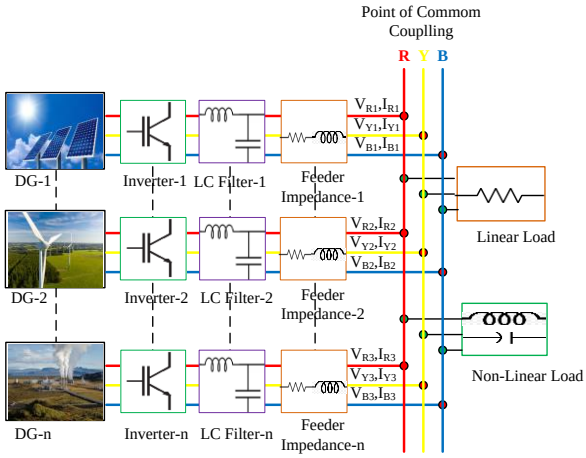

Fig. 1 A schematic representation of an Islanded Microgrid System (IMS)

The Figure 1 shows the overall system representation of the IMS, and its major subsystems are DG's, Inverter, LC filter, PCC and load. The PWM signals act as switching pulses for the inverter, and these pulses are modulated to form SPWM signals. The generated SPWM pulses control the inverter switches to produce the required AC output with desired amplitude and frequency, but they may also introduce high-frequency harmonic components. Therefore, filters such as LC filters are used to reduce these harmonics and smooth the waveform [17]. As a result, the Microgrid receives a clean, sinusoidal and stable voltage suitable for supplying loads. Hence, a suitable controller is required for proper switching of the inverter.

2.1. Principle of Operation of IMS

The primary objective of an islanded Microgrid is to maintain voltage and frequency at desirable levels at PCC despite changes in load or power generation. As the IMS operates independently, it needs to continuously monitor its

internal conditions and adjust the output of the DGs in response to variations in load ensures power quality. This necessitates the use of different control techniques to suppress harmonic distortion.

Maintaining voltage and frequency levels is a significant challenge in IMS because of different levels of DG's fluctuations arise from changes in power generation, load variations, and system stability [17, 18]. Hence, poor power quality caused by harmonic distortion, flickering, notching, etc., is also a major issue, particularly when non-linear loads introduce harmonics that affect system performance and equipment. Additionally, the system is sensitive to line impedance and variations in parameters, where slight changes can disrupt power sharing and stability. Due to these, maintaining stability under dynamic conditions requires advanced control strategies and proper coordination between all DGs.

2.2. Mathematical Modelling of IMS

Consider a typical configuration of IMS with 'n' number of DGs are connected in parallel as shown in Figure 1, and the ith DG of IMS as shown in Figure 2, along with its supporting subsystem such as LC filter, inverter, and feeder impedance.

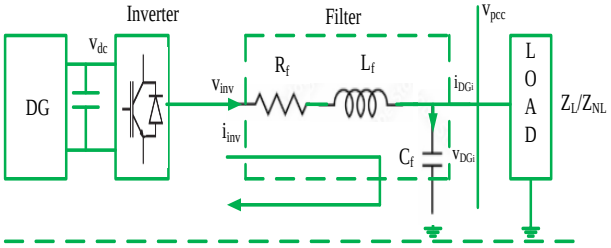

Fig. 2 Schematic diagram of ith subsystem of IMS

The KVL equation for the ith subsystem may be written [19, 20] as;

$$L_f \frac{di_{inv}}{dt} = v_{inv} - V_{DGi} - R_f i_{inv} \quad (1)$$

Voltage across the inverter is equal to the sum of voltage drop of the filter and the voltage at PCC.

Where, R_f = Filter Resistance in Ω, L_f = Filter Inductance in mH, C_f = Filter Capacitance μF, i_{inv}=Inverter Current in A, v_{inv}= m v_{DC} =Inverter voltage in V, m= Duty ratio of the inverter switch, v_{DGi} = Output Voltage of DG in V, v_f = Fundamental Voltage in V, v_h^p = p^{th} DG harmonic voltage in V.

Inverter current is the sum of current flowing through the capacitor and the load.

$$c_f \frac{dv_{DGi}}{dt} = i_{inv} - i_{DGi} \quad (2)$$

From the Equations (1) & (2)

$$\frac{d^2 v_{DGi}}{dt^2} = \frac{1}{C_f L_f} v_{inv} - \frac{1}{C_f L_f} v_{DGi} - \frac{R_f}{L_f}\frac{dv_{DGi}}{dt} - \frac{R_f}{C_f L_f} i_{DGi} - \frac{1}{c_f}\frac{di_{DGi}}{dt} \quad (3)$$

Equation (3) describes the mathematical model of a single-phase LC filter inverter. The second-order differential equation shows the relation in between DC link voltage, output voltage of DG and differentiation of load current. The state space model for IMS can be derived as [26];

Let us consider the state variables of the IMS are v_{DGi} and $\dot{v}_{DGi}$, i.e.,

$$x_1 = v_{DGi} \text{ and } x_2 = \dot{x}_1 = \dot{v}_{DGi} \quad (4)$$

$$X = \begin{bmatrix} x_1 \\ x_2 \end{bmatrix} \text{ is state vector} \quad (5)$$

Then Equation (3) can be rewritten as

$$\dot{x}_2 = -\frac{1}{C_f L_f} x_1 - \frac{R_f}{L_f} x_2 + \frac{1}{C_f L_f} v_{inv} + h(x,t) \quad (6)$$

Where $h(x,t) = -\frac{R_f}{C_f L_f} i_{DGi} - \frac{1}{c_f}\frac{di_{DGi}}{dt}$

The state-space model of the system can be written as

$$\dot{X} = AX + Bu + h(x,t) \quad (7)$$

$$Y = CX \quad (8)$$

Where (X), (Y) and (u) denote the state, output, and control-input vectors, respectively. Where (A), (B), and (C) represent the system, input, and output matrices, respectively and h(x, t) = External disturbance.

State-space model in matrix form

$$\begin{bmatrix} \dot{x}_1 \\ \dot{x}_2 \end{bmatrix} = \begin{bmatrix} 0 & 1 \\ -\frac{1}{C_f L_f} & -\frac{R_f}{L_f} \end{bmatrix} \begin{bmatrix} x_1 \\ x_2 \end{bmatrix} + \begin{bmatrix} 0 \\ \frac{1}{C_f L_f} \end{bmatrix} u + \begin{bmatrix} 0 \\ 1 \end{bmatrix} h(x,t) \quad (9)$$

Where State matrix A = $\begin{bmatrix} 0 & 1 \\ -\frac{1}{C_f L_f} & -\frac{R_f}{L_f} \end{bmatrix}$, Input matrix B = $\begin{bmatrix} 0 \\ \frac{1}{C_f L_f} \end{bmatrix}$, Output matrix C = [1 0].

3. Existing Control Strategies for IMS

The combined implementation of CDC and ERPDC along with hysteresis voltage control effectively works in islanded microgrid systems, particularly under nonlinear load conditions. In IMS, CDC generates fundamental voltage by changing the droop coefficients such as m_i, n_i, and enables power among parallel-connected distributed generators without a communication link [7].

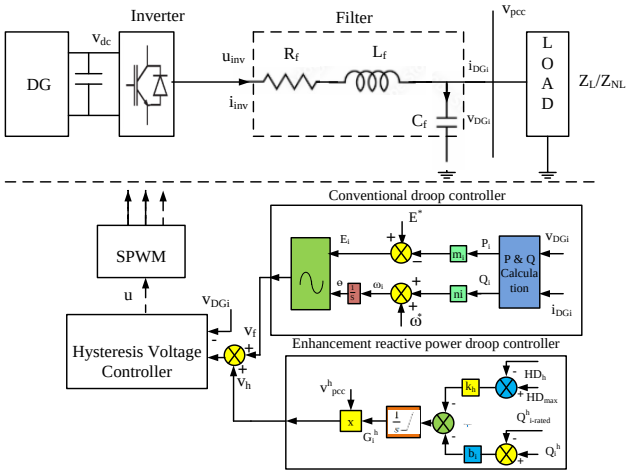

Fig. 3 Configuration of hysteresis voltage controller integrated with CDC and ERPDC

The v_{DGi} and i_{DGi} are the voltages and currents at PCC, and the Conventional droop characteristics are described as follows from Figure 3. The instantaneous power components delivered by each inverter to the PCC are expressed in terms of active and reactive power as follows from [14] is,

$$P_i = \frac{E_i\, v_{DGi} \cos\delta_i - v_{DGi}^2}{R_{0i}} \tag{10}$$

$$Q_i = -\frac{E_i\, v_{DGi}}{R_{0i}} \sin\delta_i \tag{11}$$

$$E_i = E^* - m_i P_i \tag{12}$$

$$\theta = \int \omega_i\, t = \int (\omega^* + n_i Q_i) dt \tag{13}$$

$$v_f = E_i \angle\theta = |E_i| \angle\theta \tag{14}$$

Substitute (12) Equation in (10)

$$P_i = \frac{(E^* - m_i P_i)\, v_{DGi} \cos\delta_i - v_{DGi}^2}{R_{0i}} \tag{15}$$

Rearranging the above equation

$$P_i = \frac{E^*\, v_{DGi} \cos\delta_i - v_{DGi}^2}{R_{0i} + m_i P_i \cos\delta_i} \tag{16}$$

P_i is inversely affected by the droop coefficient m_i. Higher m_i affects the lower power sharing, and vice versa.

Substitute (12) Equation in (11)

$$Q_i = -\frac{(E^* - m_i P_i)\, v_{DGi}}{R_{0i}} \sin\delta_i \tag{17}$$

$$Q_i = -\frac{(E^*\, v_{DGi} \sin\delta_i)}{R_{0i}} + \frac{(m_i P_i\, v_{DGi} \sin\delta_i)}{R_{0i}} \tag{18}$$

So Q_i is indirectly coupled with P_i and m_i and $m_i = \frac{E^* - E_i}{P_i}\ \frac{\text{Volts}}{\text{Watt}}$ & $n_i = \frac{\omega_i - \omega^*}{Q_i}\ \frac{\text{rad}/\text{sec}}{\text{Var}}$

Where E_i is the magnitude of fundamental voltage v_f in V, and integration of ω_i is angle of the fundamental voltage v_f in radians, where is P_i and Q_i are the instantaneous active and reactive powers drawn from PCC in W and Var, and E^* is rated voltage of DG in V, ω^* is rated angular frequency of PCC in r/s , E_i is the ith DG reference voltage in V, ω_i is i^{th} DG reference angular frequency, m_i and n_i are the droop coefficients of P_i and Q_i and the summary model in [7].

The fifth and seventh harmonics are particularly significant in three-phase nonlinear-load systems because they represent the first characteristic harmonics generated by six-pulse power-electronic converters. The characteristic harmonic orders of an ideal six-pulse converter are given by $(h = 6k \pm 1)$, resulting in the 5th and 7th harmonics form (k=1). These low-order harmonics can contribute significantly to current distortion, additional losses, heating, and torque pulsations in electrical equipment. Therefore, effective suppression of the 5th and 7th harmonics is an important objective in nonlinear-load harmonic compensation. In IMS, ERPDC captures the fifth and seventh harmonic voltages by adjusting the b_i and k_h as shown in Figure 3 [16].

The control signal generated by the HVC integrated with the CDC and ERPDC controller is used as the reference modulating signal for SPWM generation. Whenever the reference magnitude is higher than the carrier, the respective switch is activated; otherwise, it remains in the OFF state. In case of sinusoidal pulse width modulation, the saturation limit for DG reference voltage is given as:

$$V_{DGi_ref} \leq \sqrt{\frac{3}{2}}\,(V_{dc}/2) \tag{19}$$

$$V_{DGi_ref} = \sqrt{(v_{DGi_{ref}}^{fund})^2 + (v_{DGi_ref}^{h})^2} \tag{20}$$

The harmonic distortion of the PCC voltage at the (h)-th order is determined using the following equation.

$$HD_h = \frac{V_{pcc}^h}{V_{pcc}^{fund}} \quad (21)$$

The h-harmonic reference voltage is proportional to the negative harmonic voltage at PCC, and it can be written as:

$$V_{DGi_ref}^h \propto (-V_{pcc}^h) \quad (22)$$

$$V_{DGi_ref}^h = -G_i^h V_{pcc}^h \quad (23)$$

Where G_i^h is the proportional gain and is positive.

With Equation (21), Equation (23) can be written as

$$V_{DGi_ref}^h = -G_i^h . HD_{max} . V_{pcc}^{fund} \quad (24)$$

$$G_i^h = -\frac{V_{DGi_ref}^h}{HD_{max} . V_{pcc}^{fund}} \quad (25)$$

Substitutions of Equations (20) and (24) into inequality (19) yields the corresponding limiting values of the gain G_i^h

$$0 \le G_i^h \le \frac{\sqrt{\frac{3}{2}\left(\frac{V_{DC}}{2}\right)^2 - \left(V_{DGi}^{fund}\right)^2}}{HD_{max} V_{DGi}^{fund}} \quad (26)$$

To overcome the limitations of CDC and ERPDC, a hysteresis voltage controller is developed [21], and the overall scheme is shown in Figure 3. The reference voltage (v_r) is generated with combining CDC and ERPDC, and actual voltage (v_{DGi}) is the voltage at PCC as shown in Figure 3. The error voltage is the difference of reference voltage and actual voltage, and this error signal is then processed to the HVC controller as its input.

$$e(t) = v_r - v_{DGi} \quad (27)$$

The hysteresis band is considered as:

$$-0.1 \le e(t) \le 0.1 \quad (28)$$

This band determines, as shown in Figure 4, the allowable voltage ripple and switching frequency behavior. The switching logic is made based on the position of the error signal within the hysteresis band, and its control signal is written as:

$$u(t) = \begin{cases} 1 & e(t) > 0.1 \\ \text{no change state} & -0.1 \le e(t) \le 0.1 \\ 0 & e(t) < -0.1 \end{cases} \quad (29)$$

When the error signal exceeds the upper band, switching state of inverter is changed to reduce the output voltage. When the error signal falls below the lower band, switching state of inverter is changed to increase output voltage. The output of HVC in the form of (0,1), which drives the inverter power switches. As a result, the inverter voltage is constrained to oscillate within the predefined hysteresis boundaries around the reference value. Switching frequency depends on the width of the hysteresis band h, and load conditions.

$$f_s \propto \frac{1}{h} \quad (30)$$

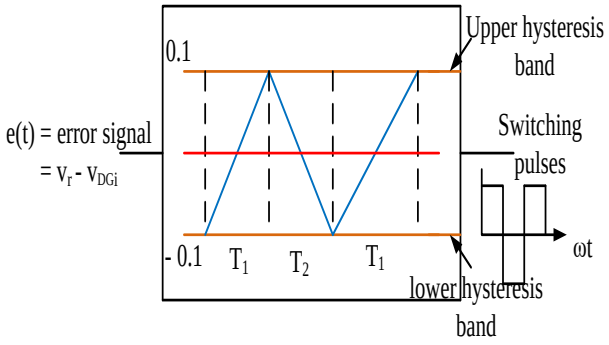

Fig. 4 Functional block diagram of hysteresis voltage control

The integration of CDC and ERPDC with hysteresis voltage control in Islanded Microgrid Systems (IMS) faces several technical challenges, such as variable switching frequency, which causes additional switching losses and thermal stress on power equipment.

In order to overcome the above challenges, it proposed to integrating STA-SMC with CDC and ERPDC, provides stronger robustness, finite-time convergence, and better voltage regulation even with parameter uncertainties. Although STA-SMC requires more complex tuning and computational effort, it significantly improves the performance in islanded Microgrid systems.

4. Development of Integrated STA-SMC with the CDC and ERPDC

The conventional droop controller generates fundamental voltage by adjusting the droop coefficients, and enhanced reactive power droop controller captures the selected harmonic voltages from the PCC, as shown in Figure 5. Existing HVC-based harmonic compensation methods combined with CDC and ERPDC mainly focus on improving harmonic suppression and dynamic tracking, but their robustness under parameter variations and disturbances remains limited. Therefore, a clear research gap exists in developing and a coordinated STA-SMC–CDC–ERPDC strategy that provides improved robustness, reduced chattering, and superior harmonic compensation compared with HVC–CDC–ERPDC approaches.

In order to improve the performance of IMS, it proposes an STA-based SMC integrated with conventional and enhanced reactive power droop controller, which processes the error signal from the PCC along with the outputs of the CDC and the ERPDC.

The error signal is the difference of voltages from PCC, i.e. v_{DGi} (actual signal) and reference voltage (v_r), which is the sum of the outputs of droop controllers, i.e. sum of v_f and v_h.

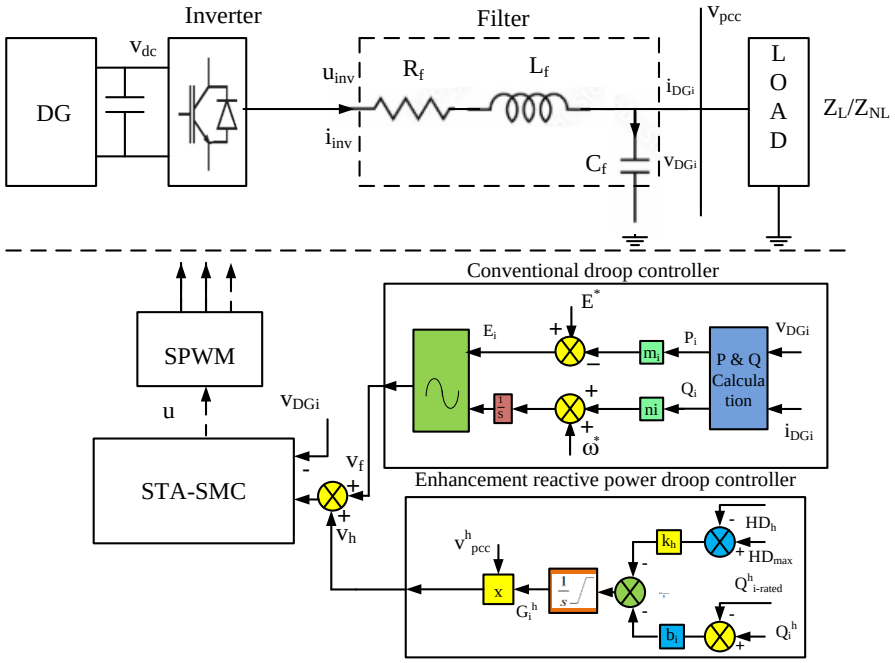

Fig. 5 Configuration of STA-SMC with CDC and ERPDC

A sliding variable is defined using the error signal and its rate of change to specify the desired dynamic behaviour of the system. The super-twisting algorithm processes this sliding variable to produce a continuous control action. Unlike classical sliding mode control, this approach avoids abrupt switching and ensures smooth control behaviour while preserving robustness against disturbances and modelling inaccuracies.

The control signal generated by the STA-SMC is supplied to the Sinusoidal Pulse Width Modulation (SPWM) as its reference input. These gating signals are applied to the inverter power switches, enabling controlled switching that converts DC power into regulated AC voltage.

4.1. Formation of Sliding Surface

The voltage error represents the difference between the reference voltage and the actual voltage, as defined by the following equation.

$$e(\text{error voltage}) = e = \underbrace{(v_r)}_{\text{reference voltage}} - \underbrace{(v_{DGi})}_{\text{actual voltage}} \quad (31)$$

Where v_r and v_{DGi} are the reference and actual voltages in V.

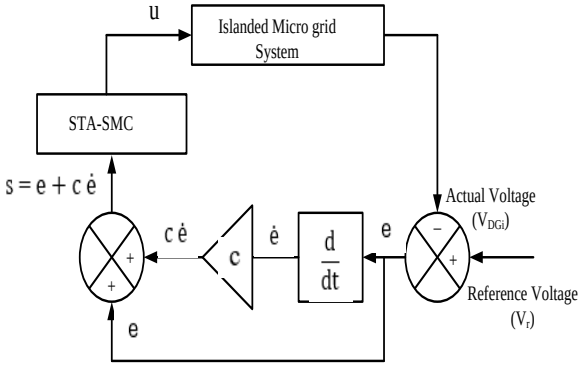

Fig. 6 Block diagram of sliding surface formation for proposed IMS

The error state variables shown in Figure 6 are defined as follows:

$$\dot{e} = \frac{d(v_r - v_{DGi})}{dt} = \dot{v}_r - \dot{v}_{DGi} \quad (32)$$

Where e and $\dot{e}$ are the error state variables, and units are V, V/S.

$$\frac{d^2e}{dt^2} = \frac{d^2V_r}{dt^2} - \frac{d^2V_{DGi}}{dt^2} \quad (33)$$

Substitute (3) Equation in (33) and rearrange,

$$\frac{d^2e}{dt^2} = \left(-\frac{1}{C_fL_f}v_{DGi} - \frac{R_f}{L_f}\frac{dv_{DGi}}{dt}\right) - \left(\frac{v_{dc}}{C_fL_f}\right)u + \left(\frac{d^2V_r}{dt^2} + \frac{R_f}{C_fL_f}i_{DGi} + \frac{1}{c_f}\frac{di_{DGi}}{dt}\right) \quad (34)$$

$$\frac{d^2e}{dt^2} = f(e) + \Delta f(e) + (b + \Delta b)u + D = \underbrace{f(e)}_{\text{non-linear system}} + \underbrace{bu}_{\text{control affine non-linear system}} + \underbrace{d}_{\text{uncertinity}} \quad (35)$$

The above equation is expressed in terms of a non-linear system, control affine non-linear uncertainty of IMS, and u is the control input.

Where $f(e) = -\frac{1}{c_fL_f}v_{DGi} - \frac{R_f}{L_f}\frac{dv_{DGi}}{dt}$, $b = -\frac{V_{DC}}{C_fL_f}$, $d = \frac{d^2V_r}{dt^2} + \frac{R_f}{C_fL_f}i_{DGi} + \frac{1}{c_f}\frac{di_{DGi}}{dt}$ (36)

The sliding surface is represented as s (e, t) = 0, where s (e, t) is a function of the system error (e) dynamic and time (t). The Sliding surface s is defined as [27]:

$$s = e + c\dot{e} \quad (37)$$

Where e (t), $\dot{e}$ (t) are the sliding surface variables, and c is coefficient of sliding surface.

In order to make sliding surface towards zero is s = 0.

$$s = 0 \Rightarrow \dot{e} = -\frac{1}{c}e \quad (38)$$

$$\frac{ds}{dt} = \frac{de}{dt} + c\frac{d^2e}{dt^2} = \frac{de}{dt} + c(f(e) + bu + d) \quad (39)$$

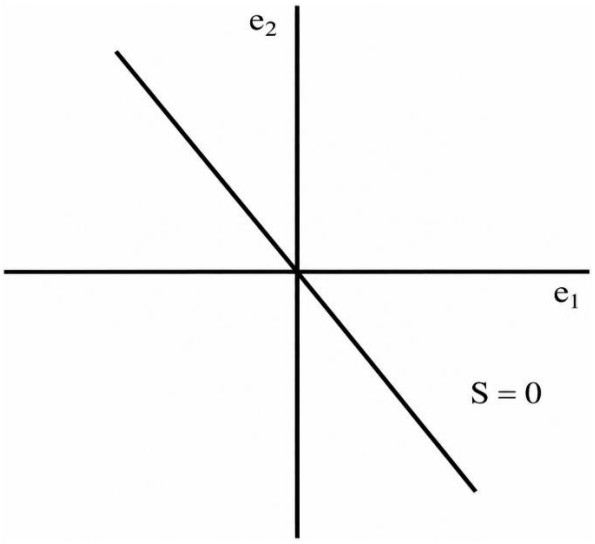

Fig. 7 Phase plane of the sliding surface

The phase-plane representation of the sliding surface shown in Figure 7 illustrates trajectory error and its derivative. The sliding surface partitions the plane into two distinct regions (i.e., $s > 0$ and $s < 0$). For each operating region, the control law generates appropriate switching actions to move the system states toward the sliding surface and satisfy the required reaching condition. As a result, trajectories originating in either region are directed toward $s = 0$.

4.2. STA-based SMC Control

The STA-SMC is a second-order sliding mode technique specifically developed to regulate nonlinear systems subjected to parameter variations, external disturbances and unmodeled dynamics. Mathematically, it realized by introducing a nonlinear control law with two adaptive terms: one integrating the sign of the sliding variable and another proportional to its fractional power.

This dual-action mechanism enables continuous and smooth control signals, effectively mitigating the chattering commonly observed in conventional sliding mode controllers. The complete internal structure of the STA-SMC is illustrated in Figure 8.

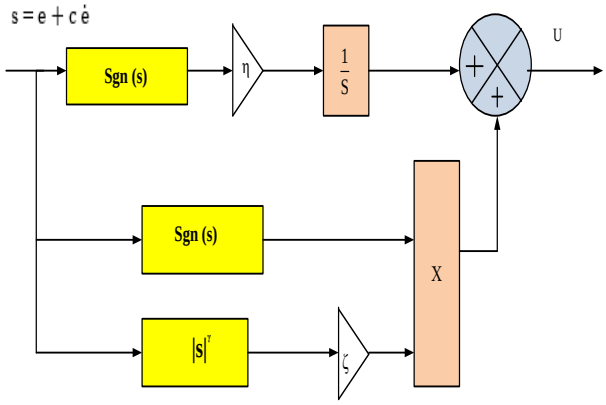

Fig. 8 Formulation of control law using STA-SMC [23, 24]

The empirical relation of STA control law [25] is considered as:

$$u = -\zeta\,|s|^{\gamma}\,\mathrm{sgn}(s) + u_1,\ \frac{du_1}{dt} = -\eta\,\mathrm{sgn}(s),\ 0 < \gamma < 1. \quad (40)$$

Where s is the sliding surface in V, $u =$ control gain signal in V, $\eta =$ robustness gain in $V^{1/2}$, $\zeta =$ damping gain in V, $\gamma =$ degree of non − linearity in V/S.

4.2.1. Reachability Condition for Convergence of Sliding Surface

The reachability condition is defined as a condition that ensures the system trajectories driven towards sliding surface from any initial state [27].

$$s\frac{ds}{dt} \leq 0. \quad (41)$$

In order to verify the reachability condition, let us recall Equation (39) by substituting the control input u given in (40) and rearranging the resulting expression yields the desired form.

$$\frac{ds}{dt} = (\dot{e} + c\, f(e) + c\, d) - (c\, b)\, \zeta\, |s|^{\gamma} sgn(s) + (c\, b)\, u_1 \quad (42)$$

A bounded function is one whose magnitude is limited by a finite positive constant. In the proposed system, the disturbances and uncertainties are assumed to be bound.

$\Theta(e,t) = (\dot{e} + c\, f(e) + c\, d)$ is bounded function, $k_1 = (c\, b)\zeta$ is gain, $v = (c\, b)u_1$ is auxiliary variable and $|\Theta(e,t)| \leq \bar{F}$ (bounded).

$$\frac{ds}{dt} = \Theta(e,t) - k_1 |s|^{\gamma} sgn(s) + v \quad (43)$$

Multiply both side of the equation by s.

$$s\frac{ds}{dt} = \Theta(e,t)s - k_1 |s|^{\gamma} s \frac{|s|}{s} + v\, s \quad (44)$$

$$= \Theta(e,t)s - k_1 |s|^{\gamma} |s| + v\, s$$

In control theory and mathematical analysis, a lemma is a supporting result or intermediate theorem used to prove a main result, such as convergence and apply the inequality Lemma function [28].

$$s\frac{ds}{dt} \leq |\Theta(e,t)||s| - |k_1||s|^{\gamma} |s| + |v||s|$$
$$\leq (|\Theta(e,t)| - |k_1||s|^{\gamma} + |v|)|s| \quad (45)$$

The selection of the design parameters c, η, ζ and γ is to satisfy the reachability condition. The parameter $c > 0$ determines the slope of the sliding surface and hence governs the error convergence rate. The robustness gain $\eta > 0$ must be selected sufficiently large to dominate bounded uncertainties, thereby ensuring the reaching condition is satisfied. The damping gain $\zeta > 0$ is introduced to attenuate oscillations and improve convergence. The exponent γ is usually chosen such that $0 < \gamma < 1$ for finite-time convergence, and it influences the nonlinearity of the control action near the origin. The control gain k_1 is selected to ensure proper convergence of the error dynamics. Specifically, when $s > 0$, the condition $sgn(s) = +ve$ is satisfied, and whens < 0, $sgn(s) = -ve$. Thereby satisfying the reachability condition $s\dot{s} \leq 0$.

Unlike conventional SMC, which suffers from chattering due to discontinuous control, the STA based approach produces a continuous control signal that ensures smooth operation. As a result, IMS has stable voltage and current regulation due to enhanced dynamic response, strong robustness against disturbances and efficient harmonic suppression.

4.3. Integrated STA-SMC with CDC and ERPDC Algorithm

To regulate the PCC voltage at the desired reference level while maintaining acceptable THD.

Step1: Obtain the system parameters for considered system

The system parameters R, L, C, v_{DC}, m_i, n_i, k_h, and b_i are to be obtained from the considered system configuration model.

Step2: Initialization and Measurements

- Initialize state variables: e(0), s(0), u(0) = 0.
- Initialize the iteration k,
- Define the convergence tolerance $\epsilon > 0$.
- Determine the gain G_i^h using the Equations (21)-(25).
- Compute outputs of CDC and ERPDC v_f and v_h using Equations (14) and (24), respectively.
- Define reference voltage:$v_r = v_f + v_h$.
- Measure the V_{DGi} from the PCC
- Compute the error signal: $e = v_r - v_{DGi}$.

Step3: Sliding surface design

$s = e + c\,\dot{e}$

- Typically, c is chosen based on system dynamics.

Step4: Control Law Design (STA-SMC)

The control input is defined as Equation (40)

$u = -\zeta |s|^{\gamma} sgn(s) + u_1$, $\frac{du_1}{dt} = -\eta\, sgn(s)$, $0 < \gamma < 1$.

The control law is designed to satisfy the reachability condition of STA-SMC.

Step 5: PCC Voltage Update

Update the PCC voltage using the system model and the compute control signal u

Step 6: Convergence Check

If

$|\, e\, | \leq \varepsilon$

The control objective is achieved, and the process is terminated.

Otherwise, repeat Steps 2-6 until the desired PCC voltage regulation is achieved.

5. Simulation Results and Discussion

The proposed controller is validated through simulation. In order to validate the performance of the proposed controller, let us consider a typical IMS system with parameters given in Table 1.

Table 1. Parameters of a typical IMS Parameters of two DGs IMS configuration

System parameters	DG1	DG2
Fundamental line Voltage(V) / frequency (Hz)	110 V/60 Hz	
Feeder Impedance	(R_1, L_1) = (0.58Ω, .05mH)	(R_1, L_1) = (0.58Ω, .05mH)
DC Voltage	220 V	220 V
Fundamental Line current	(9.44 + j 5.7708) A	
5th harmonic current source (I_{L5})	(6 – j2) A	
7th harmonic current source (IL_5)	(-5 + 0 j) A	
Total harmonic Load current (I_{Lh})	(10.44 + j 3.7708) A	
Switching frequency (f_s)	100 KHz	
m_i(V/W)	1.071×10^{-3}	1.071×10^{-3}
n_i (rad /Var)	3.768×10^{-3}	3.768×10^{-3}
Max. Harmonic distortion HD_{max}(%)	0.1%	
Rating of DG (Case: A)	3 KVA	3 KVA
$Q^h_{i_{rated}}$(Var) (Same rating)	350	350
b_i (1/Var) (same rating)	0.08	0.08
Rating of DG (Case: B)	3 KVA	1.5 KVA
$Q^h_{i_{rated}}$(Var) (different rating)	500	250
b_i (1/Var) (different rating)	0.08	0.08
STA-SMC	η=0.5, ζ=0.1, γ=0.5.	η=0.5, ζ=0.1, γ=0.5.

A 110 V/60 Hz system is selected as a practical low-voltage benchmark for evaluating the proposed harmonic-compensation controller. It enables clear analysis of low-order harmonics, particularly the 5th and 7th harmonics, and provides a suitable basis for assessing steady-state and dynamic performance.

The simulation is carried out over a 5-second time interval. DG_1 is initially connected to the PCC at t = 0 s, followed by the connection of DG_2 at t = 0.5 s. A linear load is introduced at the PCC at t = 1 s, while a nonlinear load is added at t=1.5 s. Thus, the loads are connected at the PCC and are shared by the DGs, rather than being connected to individual DG units.

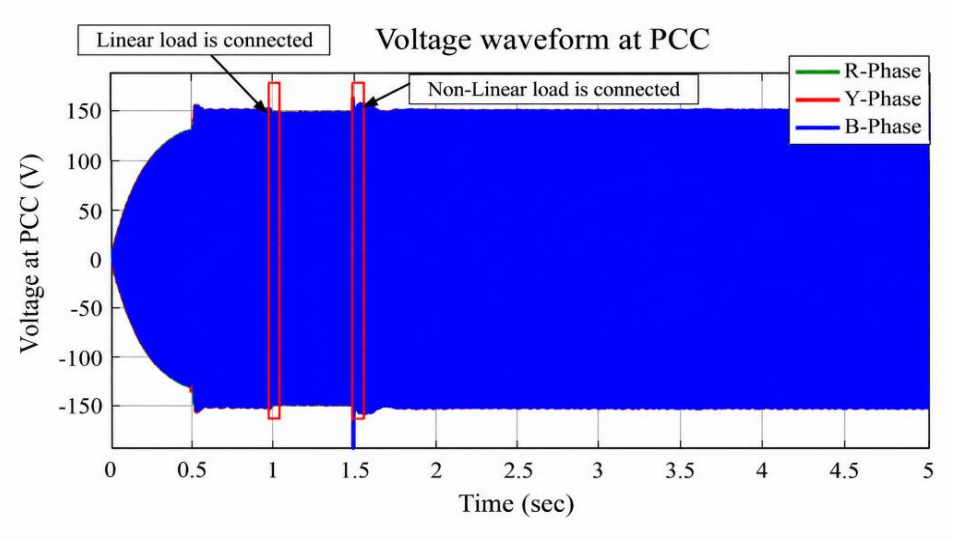

Fig. 9 Three-Phase voltages at point of common coupling

The IMS is connected with both linear and nonlinear loads, and the resultant voltage waveform at PCC as shown in Figure 9. The simulation is carried out for a total duration of 5 seconds. At 1.5 seconds, both CDC and ERPDC are applied with the STA-SMC. The effect of the controllers is observed during the transition period, and 2.5 seconds onwards, the three-phase voltage at the PCC becomes sinusoidal.

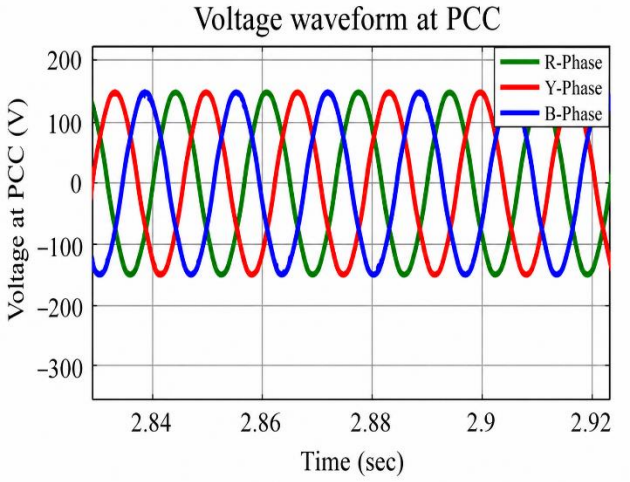

Fig. 10 Zoom view of three -phase voltages at point of common coupling

Figure 10 illustrates the zoomed view of the three-phase voltages at the PCC. It can be observed that the 3-phase voltages are balanced, sinusoidal, and maintained at the desired reference level, demonstrating the effective voltage regulation capability of the proposed STA-SMC integrated control strategy.

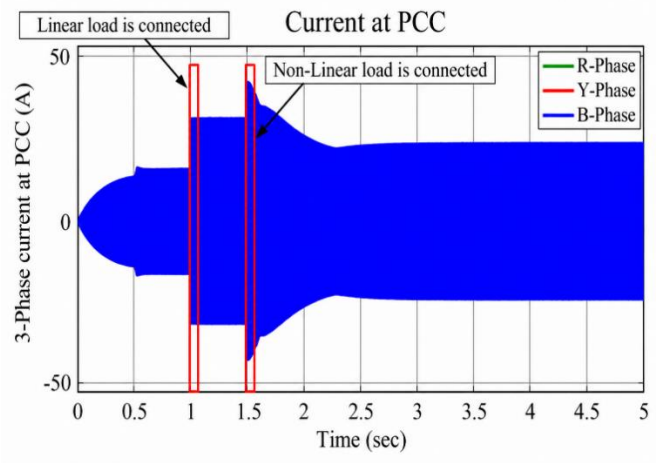

Fig. 11 Three-Phase current at point of common coupling

The activation of CDC and ERPDC controllers with STA-SMC occurs at 1.5 s. As shown in Figure 11, the 3-phase PCC current achieves a steady operating condition beyond 2.5 s. These results verify the capability of the proposed controllers to regulate harmonic current distribution effectively and ensure equitable sharing among the distributed generators.

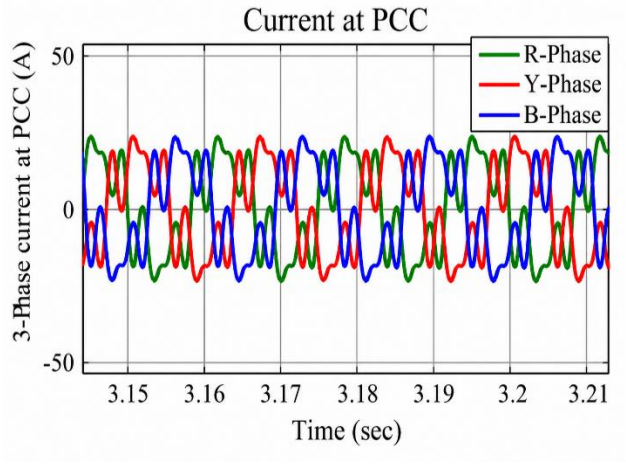

Fig. 12 Zoomed view of three-phase current at point of common coupling

The zoomed view of the three-phase currents at the PCC as sown in Figure 12. The figure also demonstrates reduced harmonic distortion and improved current quality at the PCC under the implemented STA-SMC integrated control approach.

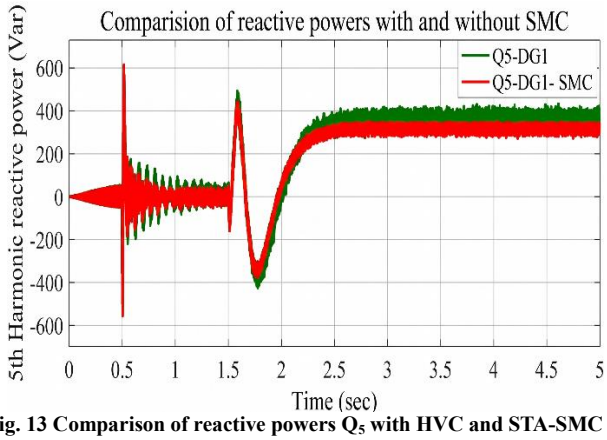

Fig. 13 Comparison of reactive powers Q_5 with HVC and STA-SMC of DG_1

The integration of HVC with conventional droop control and ERPDC, along with the STA-SMC-based scheme incorporating CDC and ERPDC, is implemented separately to compare performance. In Figure 13, the fifth-harmonic reactive power of DG_1 is presented for both control strategies.

The results indicate that the HVC based method stabilizes at 400 Var, whereas the proposed STA-SMC-based approach achieves a lower steady-state value at 300 Var, indicating improved steady-state performance.

HVC combined with conventional droop controller and enhanced reactive power droop control, and the STA-SMC scheme integrated with CDC and ERPDC, are implemented independently for comparison. The 5th harmonic reactive power of DG_2 under these strategies as shown in Figure 14.

The HVC-based configuration settles at 400 Var, whereas the STA-SMC based method reaches a lower steady-state value at 300 Var.

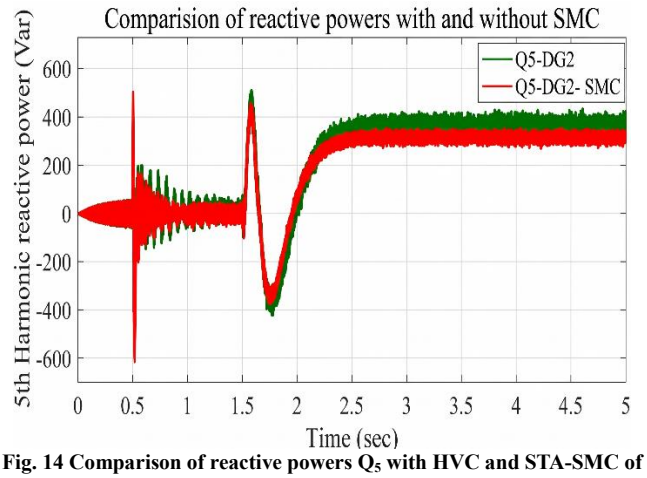

Fig. 14 Comparison of reactive powers Q_5 with HVC and STA-SMC of DG_2

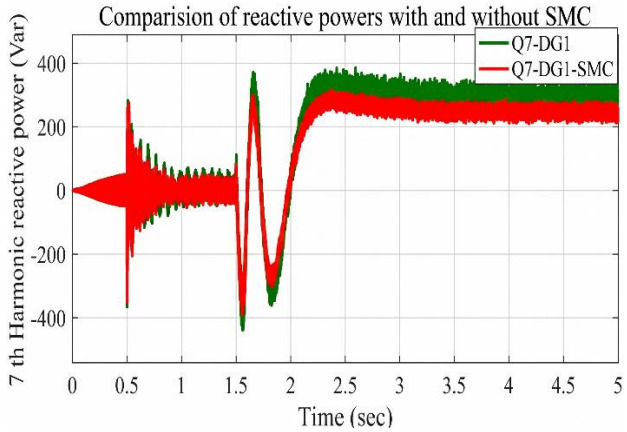

Fig. 15 Comparison of reactive power Q_7 with HVC and STA-SMC of DG_1

The integration of HVC with CDC and ERPDC, along with the STA-SMC based scheme incorporating CDC and ERPDC, is implemented separately to compare performance. In Figure 15, the seventh-harmonic reactive power of DG_1 is presented for both control strategies.

The results indicate that the HVC-based method stabilizing at 360 Var, while the STA-SMC-based approach attains a lower steady-state value at 300 Var.

HVC combined with CDC and ERPDC, and the STA-SMC scheme integrated with CDC and ERPDC, are implemented independently for comparison. As shown in Figure 16, the 7th harmonic reactive power of DG_2 under these strategies, the HVC based configuration settles at 360 Var, whereas the STA-SMC based method reaches a lower steady-state value at 300 Var.

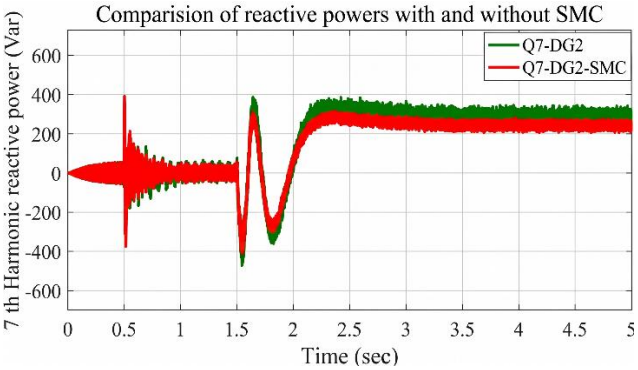

Fig. 16 Comparison of reactive power Q_7 with HVC and STA-SMC of DG_2

5.1. Same Ratings of DGs (Case A)

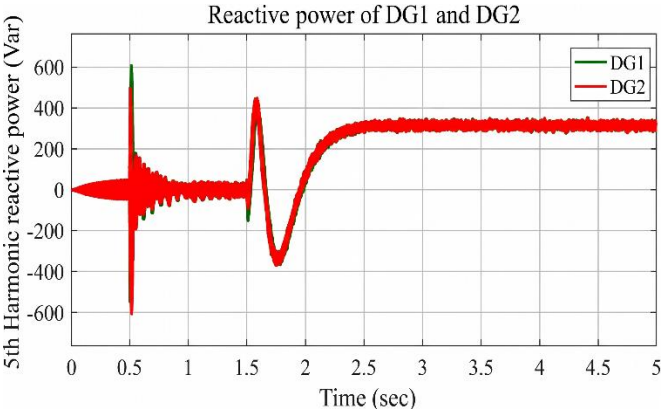

Fig. 17 Case: Reactive power Q_5 of DG_1 and DG_2 with STA-SMC controller

The fifth-harmonic reactive power response of DG_1 and DG_2 under the STA-SMC with CDC and ERPPDC is illustrated in Figure 17. It can be seen that both sources share the contribution evenly, each at 300 VAR.

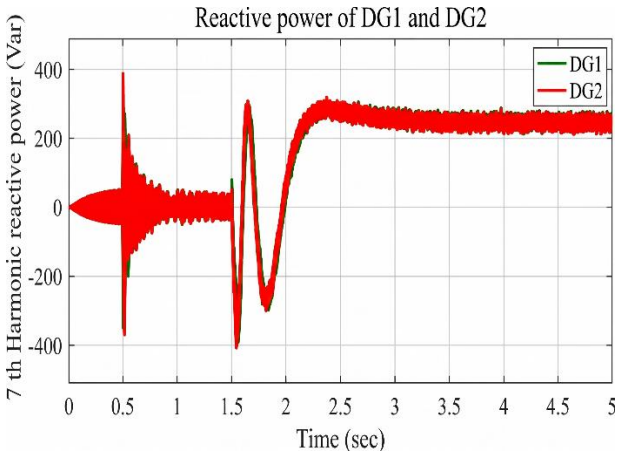

Fig. 18 Case: A reactive powers Q_7 of DG_1 and DG_2 with STA-SMC controller

The seventh-harmonic reactive power characteristics of DG_1 and DG_2 under the STA-SMC with CDC and ERPDC

scheme are depicted in Figure 18. It is observed that both generators distribute the reactive power evenly, each reaching a steady-state value 240 Var. This confirms the capability of the proposed control strategy to ensure uniform harmonic current sharing among the DG units.

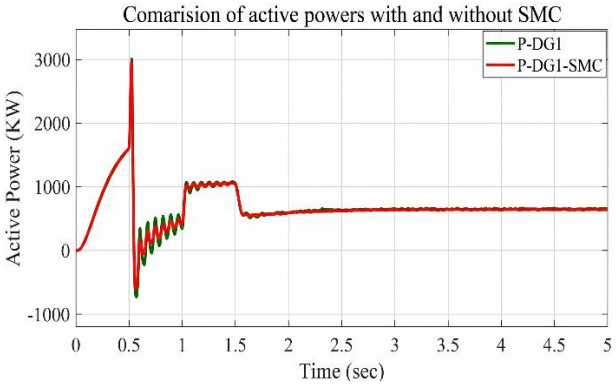

Fig. 19 DG_1 active power comparison with HVC and STA-SMC

In Figure 19, active power output of DG_1 is shown. Initially increases to 1500 W and then reduces to 1000 W before gradually declining to 500 W by 1 s, with noticeable oscillations during this interval. At 1 s, the power rises again to 1000 W, followed by a drop to 600 W at 1.5 s. During these transient conditions, the STA-SMC module effectively attenuates oscillations, ensuring smoother power transitions.

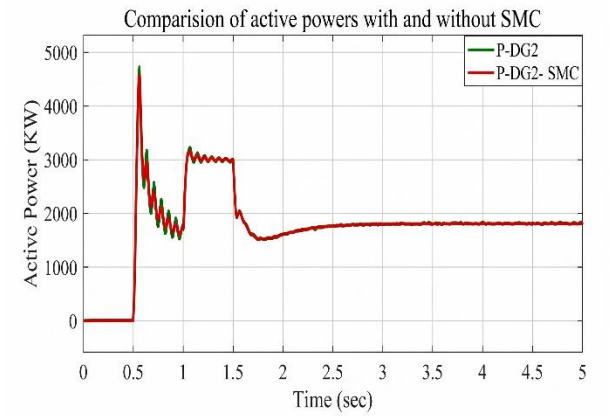

Fig. 20 DG_2 active power comparison with HVC and STA-SMC

The apparent power output of DG_2, as illustrated in Figure 20, is initially 0 W since the unit is disconnected from the system. After connection, P_2 rises to 4 kW and then gradually decreases to 1700 W by 1 s. At 1 s, the power increases again to 3 kW, followed by a reduction to approximately 1.8 kW at 1.5 s.

5.2. Different Ratings of DGs (Case B)

The STA-SMC scheme integrated with CDC and ERPDC is examined under unequal reactive power ratings of the DG units. As shown in Figure 21 and Figure 22, the fifth- and seventh-harmonic reactive powers are distributed between DG_1 and DG_2 in accordance with their assigned ratings. For the fifth harmonic, DG_1 and DG_2 supply at 200 Var and 100 Var, respectively, while for the seventh harmonic, the contributions are 180 Var for DG_1 and 100 Var for DG_2.

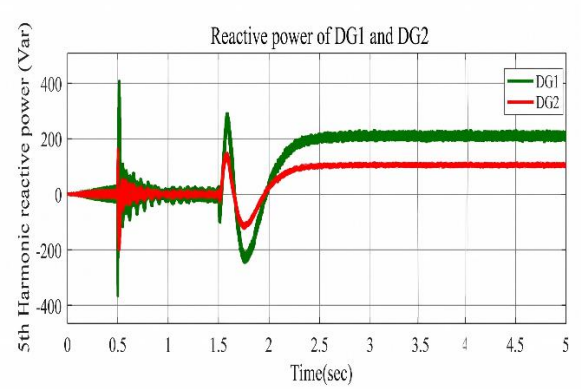

Fig. 21 Case: B reactive powers Q_5 of DG_1 and DG_2 with STA-SMC controller (different harmonic reactive power rating)

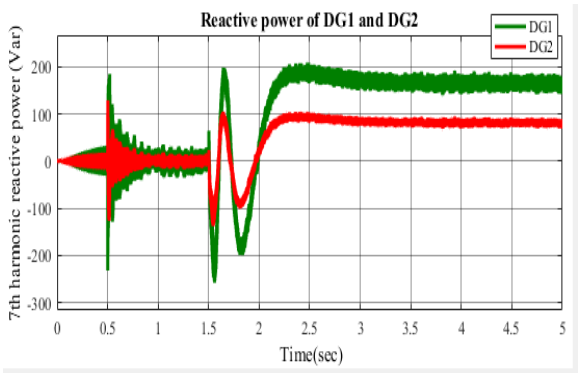

Fig. 22 Case: B reactive powers Q_7 of DG_1 and DG_2 with STA-SMC controller (different harmonic reactive power rating)

This demonstrates that the controller effectively allocates harmonic reactive power based on the specified ratings of the DGs. The THDs of the PCC voltage and current at 0.6sec (transient state) without non-linear load and are presented in Figure 23 (a) With HVC, (b) With STA-SMC module, (c) THD of Current waveform at PCC. The total harmonic distortion of the voltage is reduced from 4.28% to 2.65%. A comparative table with ripple factor and the THDs is presented in Table 2.

Table 2. Performance of proposed scheme compared with existing controller

Name of the parameter	HVC	STA-SMC
PDG_1 ripple	6.7%	2.9%
PDG_2 ripple	3.3%	1.3%
QDG_1 ripple	66.6%	6.83%
QDG_2 ripple	60.8%	6%
Overshoot	74.4%	66.7%
Settling time	0.06 sec	0.02 sec
PCC voltage THD	4.28%	2.65%

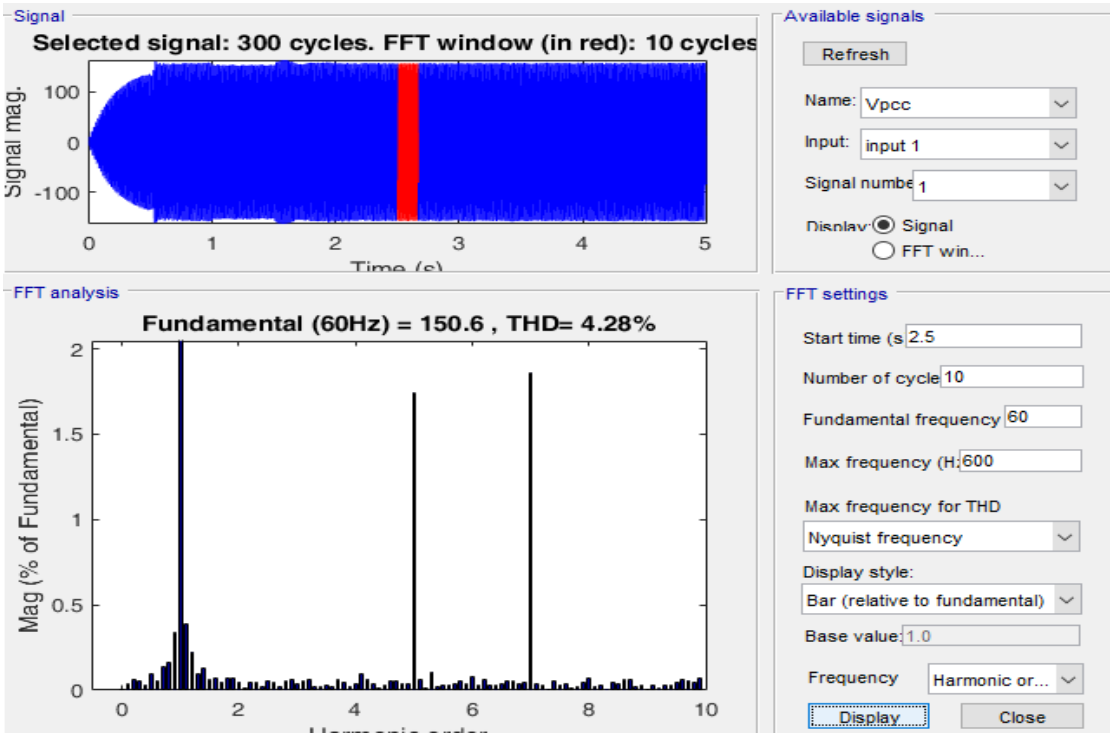
Signal
Selected signal: 300 cycles. FFT window (in red): 10 cycles
Signal mag.
Time (s)
Available signals
Refresh
Name: Vpcc
Input: input 1
Signal numbe 1
Display: Signal
FFT win...
FFT analysis
Fundamental (60Hz) = 150.6 , THD= 4.28%
Mag (% of Fundamental)
FFT settings
Start time (s 2.5
Number of cycle 10
Fundamental frequency 60
Max frequency (H 600
Max frequency for THD
Nyquist frequency
Display style:
Bar (relative to fundamental)
Base value 1.0
Frequency Harmonic or...
Display
Close

(a)

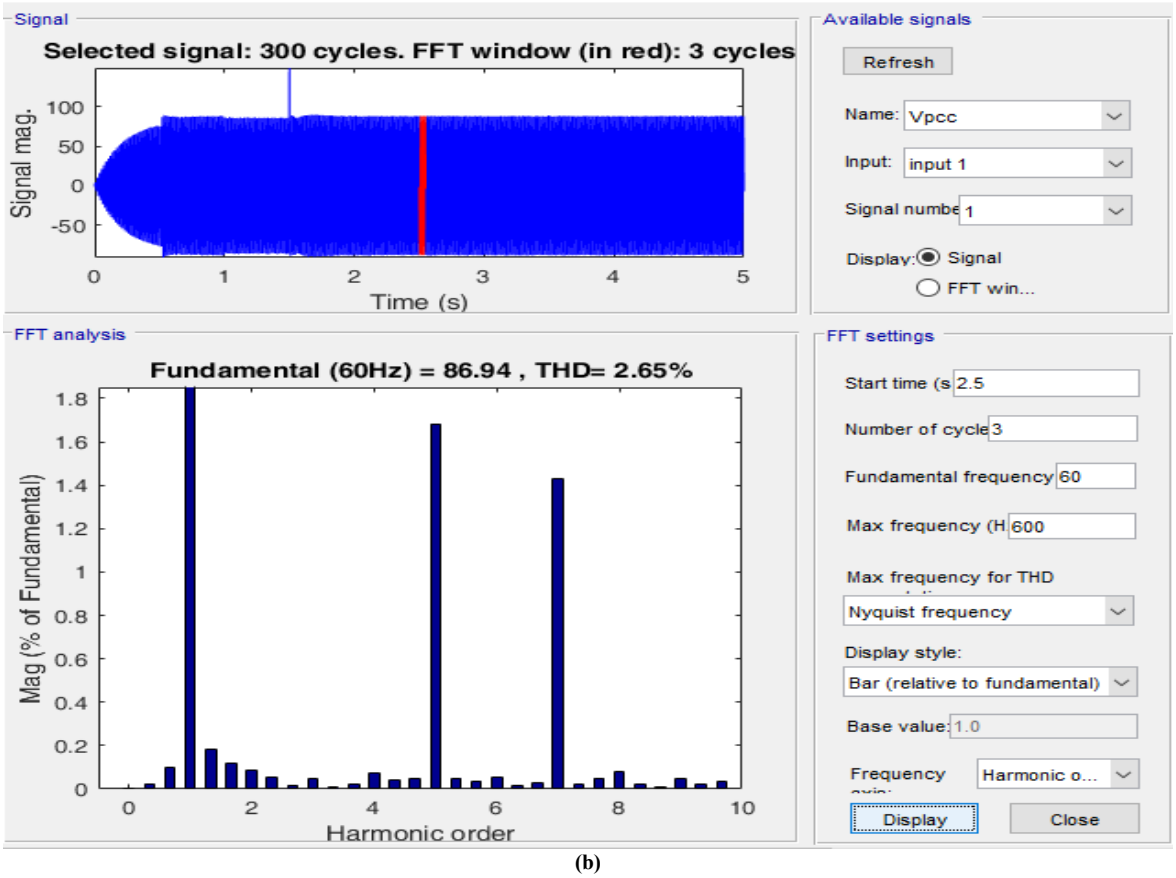
Signal
Selected signal: 300 cycles. FFT window (in red): 3 cycles
Signal mag.
Time (s)
Available signals
Refresh
Name: Vpcc
Input: input 1
Signal numbe 1
Display: Signal
FFT win...
FFT analysis
Fundamental (60Hz) = 86.94 , THD= 2.65%
Mag (% of Fundamental)
Harmonic order
FFT settings
Start time (s 2.5
Number of cycle 3
Fundamental frequency 60
Max frequency (H 600
Max frequency for THD
Nyquist frequency
Display style:
Bar (relative to fundamental)
Base value 1.0
Frequency Harmonic o...
Display
Close

(b)

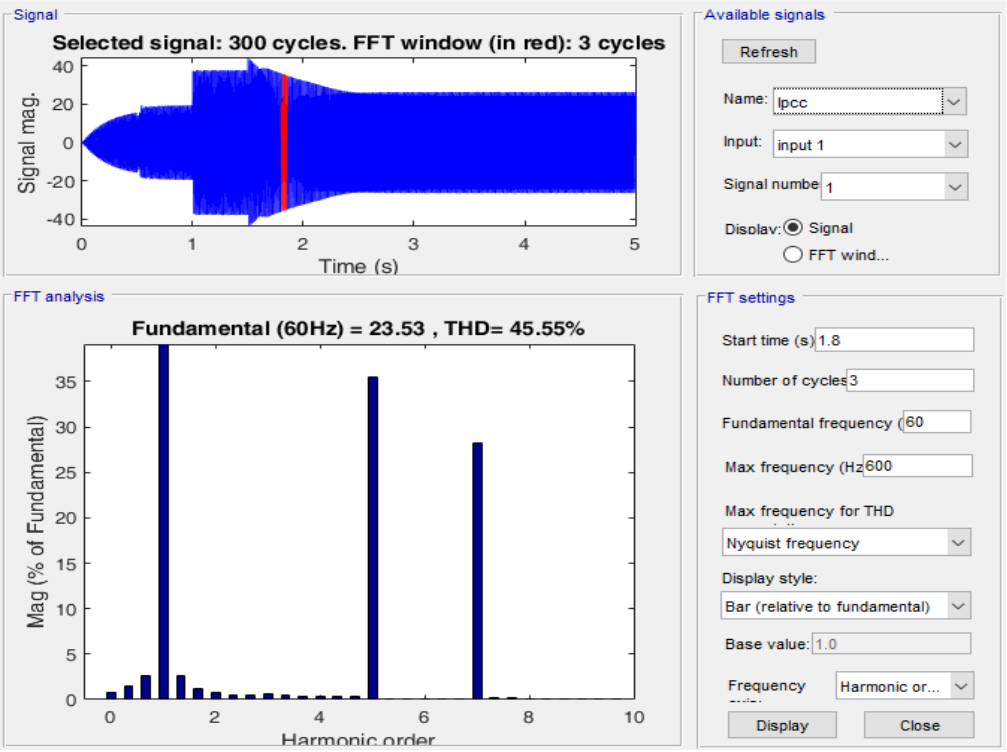

(c)

Fig. 23 THD comparison of PCC voltage (a) With HVC, (b) With STA-SMC, and (c) THD of Current waveform at PCC.

Table 2 compares the proposed control scheme with the existing controller based on the active and reactive power ripple factors of DG_1 and DG_2, voltage overshoot, settling time, and PCC voltage THD. The comparative results demonstrate that the proposed controller provides superior overall performance, with improved power-sharing characteristics, faster settling, and lower harmonic distortion at the PCC.

6. Conclusion

Islanded Microgrid comprising two DGs and a mix of linear and nonlinear loads has been modelled and evaluated in MATLAB simulation. Each DG unit was configured with dedicated filters aimed at mitigating enticing harmonics. The proposed controller handles the impact of enticing harmonics, finite-time convergence by employing a non-linear sliding surface. This integrated controller significantly suppressed oscillatory behaviour, thereby enhancing dynamic stability and improving the steady-state performance of the inverters. The improved framework achieved a substantial reduction in the THD of voltage at the PCC 2.65%, which directly contributed to enhance power quality across the system. Performance results obtained under both controllers indicate that incorporating STA-SMC provides improved overall system behavior compared with its absence. Overall, the developed STA-SMC incorporated with the conventional and enhanced reactive power droop control provides an effective and robust solution for reliable Islanded Microgrid operation under different load conditions.

Nomenclature

CDC	Conventional Droop Controller
ERPDC	Enhancement Reactive Power Droop Control
IMS	Islanded Microgrid System
PCC	Point of Common Coupling
DGs	Distributed Generators
STA-SMC	Super Twisting Algorithm based Sliding Mode Control
HVC	Hysteresis Voltage Controller
SPWM	Sinusoidal Pulse Width Modulation
THD	Total Harmonic Distortion
HD_h	h-Harmonic Distortion

References

[1] Yasir Khan, and Fang Liu, "Consumption of Energy from Conventional Sources a Challenge to the Green Environment: Evaluating the Role of Energy Imports, and Energy Intensity in Australia," *Environmental Science and Pollution Research*, vol. 30, no. 9, pp. 22712-22727, 2022. [CrossRef] [Google Scholar] [Publisher Link]

[2] Montaser Abdelsattar et al., "Energy Management of Microgrid with Renewable Energy Sources: A Case Study in Hurghada Egypt," *IEEE Access*, vol. 12, pp. 19500-19509, 2024. [CrossRef] [Google Scholar] [Publisher Link]

[3] Ramazan Bayindir et al., "Effects of Renewable Energy Sources on the Power System," *2016 IEEE International Power Electronics and Motion Control Conference (PEMC)*, Varna, Bulgaria, pp. 388-393, 2016. [CrossRef] [Google Scholar] [Publisher Link]

[4] Moslem Uddin et al., "Microgrids: A Review, Outstanding Issues and Future Trends," *Energy Strategy Reviews*, vol. 49, pp. 1-16, 2023. [CrossRef] [Google Scholar] [Publisher Link]

[5] Adriel M. Rizzato Lede et al., "Microgrid Architectures for Distributed Generation: A Brief Review," *2017 IEEE PES Innovative Smart Grid Technologies Conference-Latin America (ISGT Latin America)*, Quito, Ecuador, pp. 1-6, 2017. [CrossRef] [Google Scholar] [Publisher Link]

[6] Vannesa Quintero-Molina et al., "Power Quality in AC Islanded Microgrids: Technical Framework and State of the Art Review," *Engineering and Research*, vol. 40, no. 3, pp. 29-37, 2020. [Google Scholar]

[7] Ghazanfar Shahgholian, Mohammadreza Moradian, and Arman Fathollahi "Droop Control Strategy in Inverter-based Microgrids: A Brief Review on Analysis and Application in Islanded Mode of Operation," *IET Renewable Power Generation*, vol. 19, no. 1, pp. 1-19, 2025. [CrossRef] [Google Scholar] [Publisher Link]

[8] Kuang-Hsiung Tan, Meng-Yang Li, and Xiang-Yu Weng, "Droop Controlled Microgrid with DSTATCOM for Reactive Power Compensation and Power Quality Improvement," *IEEE Access*, vol. 10, pp. 121602-121614, 2022. [CrossRef] [Google Scholar] [Publisher Link]

[9] Ahmed M. Abouassy et al., "An Improved Droop-based Adaptive Virtual Impedance for Accurate Power Sharing Among Multiple DGs in Islanded Microgrid," *IEEE Access*, vol. 13, pp. 108918-108933, 2025. [CrossRef] [Google Scholar] [Publisher Link]

[10] Min Ding et al., "Parallel Operation Strategy of Inverters based on an Improved Adaptive Droop Control and Equivalent Input Disturbance Approach," *Electronics*, vol. 13, no. 3, pp. 1-14, 2024. [CrossRef] [Google Scholar] [Publisher Link]

[11] Wei Sun et al., "Secondary Control of Islanded Microgrids with Variable Topology," *2024 IEEE 7th International Electrical and Energy Conference (CIEEC)*, Harbin, China, pp. 4170-4175, 2024. [CrossRef] [Google Scholar] [Publisher Link]

[12] Sunghyok Kim, Songchol Hyon, and Yongil An, "Harmonic Power Sharing Control using Adaptive Virtual Harmonic Impedance in Islanded Microgrids," *International Journal of Emerging Electric Power Systems*, vol. 25, no. 2, pp. 135-148, 2023. [CrossRef] [Google Scholar] [Publisher Link]

[13] Hui Hwang Goh et al., "Harmonic Virtual Impedance Control in Islanded Microgrids for Harmonic Power Sharing and Harmonic Suppression," *CSEE Journal of Power and Energy Systems*, vol. 12, no. 2, pp. 688-697, 2026. [CrossRef] [Google Scholar] [Publisher Link]

[14] Qing-Chang Zhong, "Robust Droop Controller for Accurate Proportional Load Sharing Among Inverters Operated in Parallel," *IEEE Transactions on industrial Electronics*, vol .60, no. 4, pp. 1281-1290, 2011. [CrossRef] [Google Scholar] [Publisher Link]

[15] Seyyed Yousef Mousazadeh Mousavi et al., "Autonomous Control of Current-and Voltage-Controlled DG Interface Inverters for Reactive Power Sharing and Harmonics Compensation in Islanded Microgrids," *IEEE Transactions on Power Electronics*, vol. 33, no. 11, pp. 9375-9386, 2018. [CrossRef] [Google Scholar] [Publisher Link]

[16] Hassan Moussa et al., "Voltage Harmonic Distortion Compensation with Non-Linear Load Power Sharing in Low-Voltage Islanded Microgrid," *Mathematics and Computers in Simulation*, vol. 158, pp. 32-48, 2019. [CrossRef] [Google Scholar] [Publisher Link]

[17] Tung Lam Nguyen et al., "Interconnected Microgrid Systems: Architecture, Hierarchical Control, and Implementation," *Smart Cyber-Physical Power Systems: Fundamental Concepts, Challenges, and Solutions*, vol. 1, pp. 151-165, 2025. [CrossRef] [Google Scholar] [Publisher Link]

[18] Muhammad Waseem Altaf et al., "Microgrid Protection Challenges and Mitigation Approaches-A Comprehensive Review," *IEEE Access*, vol. 10, pp. 38895-38922, 2022. [CrossRef] [Google Scholar] [Publisher Link]

[19] Hao Pan, Qingfang Teng, and Dangdang Wu, "MESO-based Robustness Voltage Sliding mode Control for AC Islanded Microgrid," *Chinese Journal of Electrical Engineering*, vol. 6, no. 2, pp. 83-93, 2020. [CrossRef] [Google Scholar] [Publisher Link]

[20] Nourhan A. Maged et al., "Optimal Super Twisting Sliding Mode Control Strategy for Performance Improvement of Islanded Microgrids: Validation and Real-Time Study," *International Journal of Electrical Power and Energy Systems*, vol. 157, pp. 1-27, 2024. [CrossRef] [Google Scholar] [Publisher Link]

[21] Precious Chungu, Francis Mulolani, and Musa Ndiaye, "A Comparative Study of the PI Controller to the Hysteresis Controller for Voltage and Current Control in Inverter-based Microgrids," *2022 IEEE PES 14th Asia-Pacific Power and Energy Engineering Conference (APPEEC)*, Melbourne, Australia, pp. 1-6, 2022. [CrossRef] [Google Scholar] [Publisher Link]

[22] Dipak Kumar Dash, Pradip Kumar Sadhu, and Alok Kumar Shrivastav, "A Robust Super Twisting Sliding Mode Controller or Optimal Grid Synchronization of Photovoltaic System," *Microsystem Technologies*, vol. 30, no. 9, pp. 1137-1151, 2024. [CrossRef] [Google Scholar] [Publisher Link]

[23] Ahyeong Choi et al., "Super-Twisting Sliding Mode Control with SVR Disturbance Observer for PMSM Speed Regulation," *Applied Sciences*, vol. 12, no. 21, pp. 1-11, 2022. [CrossRef] [Google Scholar] [Publisher Link]

[24] Dkhil Asma et al., "Robust Fractional PI Controller Design for Stand-Alone Microgrid Under Load Variation: An Optimization-based Approach," *International Journal of Renewable Energy Research (IJRER)*, vol. 13, no. 4, pp. 1526-1537, 2023. [Google Scholar]

[25] Hamza Gasmi et al., A new Scheme of the Fractional-Order Super Twisting Algorithm for Asynchronous Generator-based Wind Turbine," *Energy Reports*, vol. 9, pp. 6311-6327, 2023. [CrossRef] [Google Scholar] [Publisher Link]

[26] Mostafa Barzegar-Kalashani et al., "Robust Nonlinear Sliding Mode Controllers for Single-Phase Inverter Interfaced Distributed Energy Resources based on Super Twisting Algorithms," *ISA Transactions*, vol. 123, pp. 61-75, 2022. [CrossRef] [Google Scholar] [Publisher Link]

[27] Li Donga, and Pei Jiang, "Improved Super-Twisting Sliding Mode Control Strategy in Permanent Magnet Synchronous Motors for Hydrogen Fuel Cell Centrifugal Compressor," *Heliyon*, vol. 10, no. 2, pp. 1-12, 2024. [CrossRef] [Google Scholar] [Publisher Link]

[28] Hassan K. Khalil, and Jessy W. Grizzle, Nonlinear Systems, 3rd ed., Prentice-hall, 2002. [Google Scholar]